

# First-Principles Study of Structural Transition in $\text{LiNiO}_2$ and High Throughput Screening for Long Life Battery

Tomohiro Yoshida<sup>1</sup>, Kenta Hongo<sup>2,3</sup>, and Ryo Maezono<sup>4,5</sup>

<sup>1</sup> Department of Computer-Aided Engineering and Development,  
Sumitomo Metal Mining Co., Ltd., Minato-ku, Tokyo 105-8716, Japan

<sup>2</sup> Research Center for Advanced Computing Infrastructure,  
JAIST, Asahidai 1-1, Nomi, Ishikawa 923-1292, Japan

<sup>3</sup> PRESTO, Japan Science and Technology Agency,  
4-1-8 Honcho, Kawaguchi-shi, Saitama 322-0012, Japan

<sup>4</sup> School of Information Science, JAIST, Asahidai 1-1, Nomi, Ishikawa, 923-1292, Japan and

<sup>5</sup> Computational Engineering Applications Unit, RIKEN,  
2-1 Hirosawa, Wako, Saitama 351-0198, Japan

(Dated: December 29, 2021)

Herein, we performed *ab initio* screening to identify the best doping of  $\text{LiNiO}_2$  to achieve improved cycle performance in lithium ion batteries. The interlayer interaction that dominates the *c*-axis contraction and overall performance was captured well by density functional theory using van der Waals exchange-correlation functionals. The screening indicated that Nb-doping is promising for improving cycle performance. To extract qualitative reasonings, we performed data analysis in a materials informatics manner to obtain a reasonable regression to reproduce the obtained results. LASSO analysis implied that the charge density between the layers in the discharged state is the dominant factor influencing cycle performance.

## I. INTRODUCTION

Improvements in lithium ion batteries (LIBs) have contributed to 'clean energy' as a key technology to reduce energy consumption and have been used in mobile devices and automobiles<sup>1,2</sup>. Cathode materials of LIBs most significantly influence battery performances, especially in terms of their lifetime and safety (strength against damage and deteriorations)<sup>3-5</sup>. Significant efforts<sup>6</sup> have been made to improve these aspects beyond investigations of the conventional cathode material,  $\text{LiCoO}_2$  (LCO)<sup>7</sup>.

$\text{LiNiO}_2$  (LNO) has been shown to achieve higher energy densities during storage than that of LCO<sup>3,8-16</sup>. It has also attracted interest because Ni is cheaper than Co. The drawback of LNO is its cycle characteristics, which are relevant to the batteries' lifetime. The battery storage capacity is reduced with increasing numbers of charge-discharge cycles. After a smaller number of cycles, LNO loses its initial capacity more rapidly than the other cathode materials<sup>3,8-16</sup>. Atomic substitution has been reported as a promising strategy to improve cycle characteristics, including substituting Ni sites for Al<sup>17,18</sup>, Mg<sup>19-21</sup>, Co<sup>22-24</sup>, Mn<sup>25,26</sup>, Fe<sup>27</sup>, Y<sup>28</sup>, Ti<sup>29</sup>, Zr<sup>30-32</sup>, and Na<sup>33</sup>.

When  $x$  percent of Li ions are removed from the cathode during charging, the cathode undergoes a structural transition from rhombohedral (H1) [ $x < 0.25$ ] to monoclinic (M) [ $0.25 < x < 0.55$ ], rhombohedral (H2) [ $0.55 < x < 0.75$ ], and rhombohedral (H3) [ $0.75 < x$ ]<sup>3,10,34</sup> successively. Drastic contractions along the *c*-axis occur when H2 transforms into H3, which has been identified as the major process causing deterioration during charge-discharge cycles<sup>3</sup>. These contractions accumulate internal stresses, leading to cathode cracking and allowing the

electrolyte to enter and cause further deterioration.

Differences in cycle performances between LNO and LCO can be attributed to the different values of  $x$  at the specific charging voltage, 4.2 V. This voltage is the upper bound where the highest charging performance is realized while preventing electrolyte degradation. At the voltage (4.2 V),  $x$  approaches 1.0 the H2-H3 transition inevitably occurs in LNO<sup>3,10</sup>, whereas  $x$  can be kept smaller to avoid this transition in LCO<sup>34</sup>. The cycle performance of LNO has been improved by reducing the charging voltage<sup>3</sup> via reduced  $x$  to hinder the large contractions along the *c*-axis. Nevertheless, achieving higher voltages is necessary to improve charging capacities while suppressing the *c*-axis contraction by tuning LNO.

Therefore, because the above described contraction dominates cycle performance, the computational design of the optimum doping is necessary to realize improved performance as the contraction can be easily evaluated by *ab initio* methods. A similar study was reported for  $\text{LiFePO}_4$ -based batteries, achieving drastic performance improvements<sup>35</sup>. Herein, we performed theoretical calculation to identify which doping element could result in the best cycle performance. The *c*-axis contractions were evaluated by *ab initio* methods with 32 candidate elements as the dopant to substitute the Ni sites in LNO. This high-throughput screening showed that the Nb-doping would result in the best performance.

## II. METHODS

Fig. 1 shows the unit cell we used to model the systems with dopants with a rhombohedral (R-3m) symmetry<sup>10</sup>. The cell corresponds to the  $2 \times 2 \times 1$  supercell

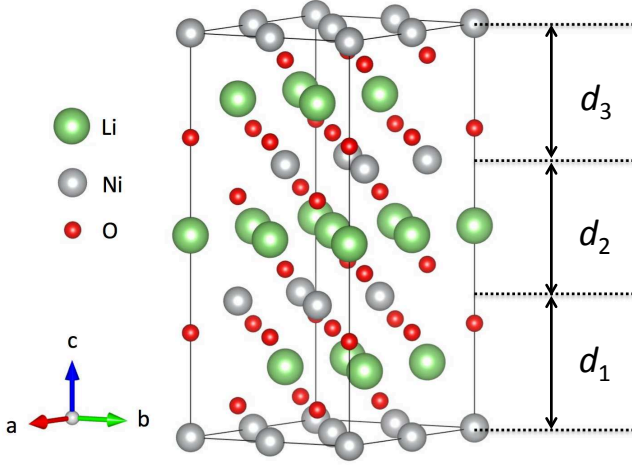


FIG. 1. The unit cell used to model the systems with dopants, with a rhombohedral ( $R\bar{3}m$ ) symmetry. The cell corresponds to the  $2 \times 2 \times 1$  supercell of the pristine  $\text{LiNiO}_2$  unit cell. Inter-layer distances,  $d_{i=1\sim 3}$ , were averaged for evaluation as a measure for composition optimization.

of the pristine  $\text{LiNiO}_2$  unit cell. The Vienna Ab initio Simulation Package (VASP)<sup>36,37</sup> was used for all density functional theory (DFT) evaluations with projector augmented wave (PAW) treatment for ionic cores. Using careful convergence tests, we used the plane wave cutoff ( $E_{\text{cut}}$ ) of 650 eV with a  $5 \times 5 \times 2$   $k$ -mesh.

For the exchange-correlation (XC) functional, we adopted optB86b-vdW<sup>38,39</sup> because conventional XC such as PBE<sup>40</sup> cannot capture the long-range binding between Ni-O layers, especially after Li ions are removed during charging. Several choices are available for the van der Waals exchange-correlation functionals (vdW-XC). For LNO, the vdW-D3<sup>41</sup> has been reported to be incapable of reproducing the contraction along the  $c$ -axis<sup>42</sup>. For LCO<sup>43</sup> it has been reported that the 'opt'-vdW-type XC well reproduce the unit cell volumes and voltages where Li ions begin desorbing, as estimated by Eq. (1). The optB86b-vdW-XC<sup>38,39</sup> was confirmed to achieve the best performance to reproduce experimental results of many systems including metallic, ionic, and covalent crystals<sup>38</sup>. As described later, we confirmed that the vdW-XC is indispensable for describing the system studied here.

### III. RESULTS AND DISCUSSION

Table I summarizes the optimized geometries and voltage at which the Li ions begin desorbing,  $V_{\text{des}}$ , estimated using different XC and compared with experimental values<sup>10,44</sup>. The desorbing voltage



can be estimated by

$$V(x_1, x_2) = -\frac{E_{\text{Li}_{x_1}\text{NiO}_2} - E_{\text{Li}_{x_2}\text{NiO}_2} - (x_1 - x_2) \cdot E_{\text{Li}}}{(x_1 - x_2) \cdot e}, \quad (1)$$

where  $E$  denotes the ground state energy of each compound. In Table I we defined  $V_{\text{des}} = V(1, 0)$ . It is clear that vdW-XC achieved better agreement with the experimental values than PBE for the geometry [(2% by vdW) vs (11% by PBE), error in  $c$  the charged state ( $\text{NiO}_2$ )], and voltage [23% vs 27%]. Interestingly, the DFT+ $U$  scheme further improved the agreement when  $U$  was introduced to Ni-3d. Using  $U = 6.7$  eV<sup>45</sup>, errors of 1% and 4% were achieved for  $c$  and  $V_{\text{des}}$ . However, the '+ $U$ ' scheme was not adopted in this study, *i.e.*, high-throughput screening. The  $c$ -length was used as the assessment function for screening and '+ $U$ ' was only improved by a negligible amount compared to the magnitude of interest (*i.e.*, the variation of  $c$  during charging). As in Fig. 2, the trend required for the assessment function was well captured even at  $U = 0$ . The most compelling reason for not including '+ $U$ ' is its high computational cost and its significantly worse convergence in a SCF (self-consistent field), rendering the screening inefficient. Furthermore, it is difficult to choose a proper  $U$  value for each system with different concentrations of Li vacancies and various possible atomic substitutions.

Fig. 2 shows the estimated lattice relaxations during the charge ( $x = 1$ )-discharge ( $x = 0$ ) process obtained using PBE and vdW-XC. For each  $x$ , relaxation calculations were performed over all possible symmetries with the Li vacancies in the unit cell (shown in Fig. 1). The plot shows the lattice parameters of the most stable structure at each  $x$  value. For the  $a$ -axis [Fig. 2(a)], both PBE and vdW-XC reproduced the trend where the lattice parameter was reduced monotonically as the system is charged, consistent with experimental observations. A remarkable contrast was observed in the  $c$ -axis [Fig. 2(b)], where PBE failed to reproduce the contraction as  $x$  increases. Up to  $x = 0.8$ , it was confirmed that at least one Li ion present within the inter-layers prevented contraction, but at  $x = 0.8$  this inter-layer appears without Li, allowing for sudden contractions. The increasing trend for  $0 < x < 0.8$  was attributed to the reduced ionic interactions caused by the charge reduction in the Ni-O layer by the oxidation of  $\text{Ni}^{3+}$  to  $\text{Ni}^{4+}$ . The large overestimations of the PBE lattice constants can be primarily attributed to the general tendency of PBE to afford underbindings<sup>46</sup>, and to the lack of vdW inter-layer attractions that only the vdW-XC considered. Since the contribution of the vdW forces to the cohesion was estimated to be approximately 1 ~ 2%<sup>47</sup>, the difference in the plot (Fig. 2) of approximately 1% is reasonable. Even with reduced ionic binding between layers, PBE yielded contractions at  $0.8 < x < 0.9$  to fill the Li vacancies between the layers. However, at  $x = 1.0$  the reduced charge eventually becomes incapable of forming ionic bonds be-

XC	$V_{\text{des}}$	$a$ (Å) (LiNiO <sub>2</sub> )	$c$ (Å) (LiNiO <sub>2</sub> )	$a$ (Å) (NiO <sub>2</sub> )	$c$ (Å) (NiO <sub>2</sub> )
PBE	3.05	2.89	14.16	2.82	14.85
vdW	3.25	2.87	14.04	2.81	13.10
Experiments <sup>10,44</sup>	4.2	2.88	14.18	2.81	13.36

TABLE I. Predictions depending on the choice of exchange-correlation functionals (XC).  $V_{\text{des}}$  denotes the Li-desorbing voltage, as defined in Eq. (1) with the optimized lattice parameters ( $a$  and  $c$ ) along the  $a$ - and  $c$ -axes.

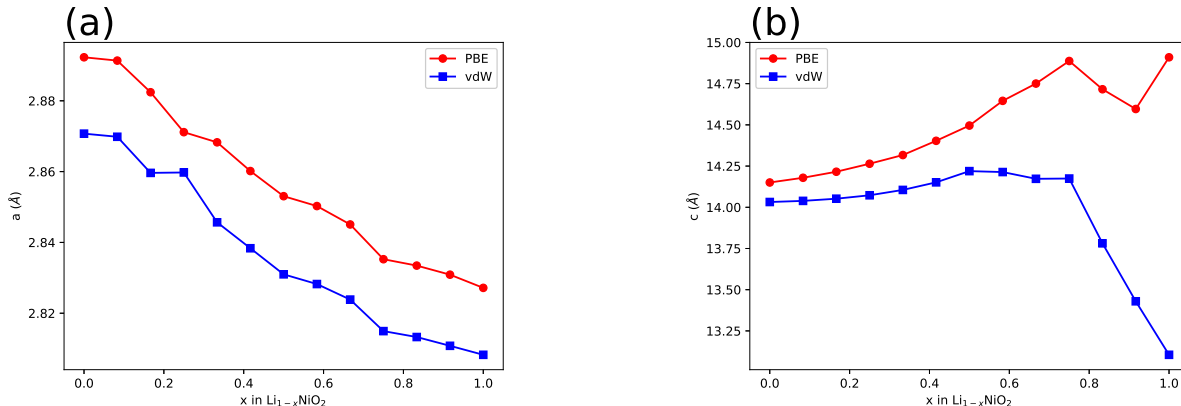


FIG. 2. Estimated lattice relaxation during the charge ( $x = 1$ )-discharge ( $x = 0$ ) process with a comparison between PBE and vdW-XC. PBE was incapable of reproducing the contraction along the  $c$ -axis during charging.

tween layers<sup>43</sup>, leading to increased inter-layer spacing. On the other hand, using vdW-XC, the binding works even with the reduced charge, reproducing the proper contractions to fill Li vacancies.

The sharp decrease in the  $c$  parameter [the blue plot in Fig. 2(b)] corresponds to the H2→H3 transition<sup>3,10</sup>. It should be noted that this change is not accompanied by any symmetric transitions, so it is not a true 'structural transition' but a 'structural change'. The main conclusion is that vdW-XC is indispensable for describing the H2→H3 process. However, previous studies<sup>42</sup> successfully employed meta-GGA to describe this process. Although meta-GGA does not include dispersion interactions explicitly, it has been reported<sup>48</sup> that it can describe vdW-like  $\sim r^{-6}$  behavior in the system. We employed vdW-XC rather than meta-GGA because the latter gives rise to worse SCF convergence<sup>49</sup>, which is fatal for high-throughput screening.

Confident of our XC choice of vdW/ $U=0$  describing the target, namely the  $c$ -axis contractions as an indicator of cycle performance, we performed high-throughput screening to determine the optimum choice of the doping element for LNO. We considered 66 doping elements, 'X', from the third row and lower in the periodic table, up to Pa (atomic number 91) and excluding those for which pseudo potentials were not available. To enhance rate capability, Co is usually doped into LNO<sup>50</sup>. We also substituted X to Ni to improve cycle performance. The ratio of elements was Ni:Co:X=0.75:0.17:0.08, *i.e.*, where two Ni sites are occupied by Co atoms, while one

Ni site is occupied by X within a unit cell, as depicted in Fig. 1. It should be noted that some ions cannot adopt a trivalent state. For example, Na only adopts a stable valence of  $\text{Na}^{+1}$ . However, to ensure charge neutrality in such cases, the valence of two Ni atoms can be changed from  $\text{Ni}^{+3}$  to  $\text{Ni}^{+4}$ . Therefore, it was assumed that all elements can be dissolved in LNO. It should be mentioned that the supercell size ( $2 \times 2 \times 1$ ) was relatively small. However, if a larger cell was considered, significant amounts of time would be necessary to determine the most stable structure. Therefore, we used the  $2 \times 2 \times 1$  supercell and will investigate larger systems using genetic algorithms or Bayesian optimization in the future. There are  ${}_{12}\text{C}_2 \times 10 = 660$  possible substitution patterns that can be achieved under the above conditions, but we can reduce these structures to 10 symmetrically different structures (see Appendix A). For these 10 possibilities, geometrical optimizations were performed to determine the most stable structure as a representative for X to be compared with the structures obtained from other X. We compared the  $c$ -axis contraction,  $\Delta d_{\text{ave}} = \sum_{i=1}^3 (d_i^d - d_i^c)/3$ , where  $d_i^d$  ( $d_i^c$ ) denotes the layer spacing, as depicted in Fig. 1 when the system is discharged (charged).

The spacing,  $d_i^c$ , of the charged state was evaluated at the 75 %-charged state, *i.e.*, the crystal structure where 9 Li ions are removed from the unit cell shown in Fig. 1. This percentage was the maximum where we could expect to maintain the charge neutrality because only  $\text{Ni}^{3+}$  to  $\text{Ni}^{4+}$  and  $\text{Co}^{3+}$  to  $\text{Co}^{4+}$  could compensate for neutral-

ity, while other ions could not due to their specific redox potentials. For the charged states, geometry optimizations were performed to determine  $d_i^c$  starting from the initial structures generated by LNO with Li vacancies.

It is well-known that the ground state of LNO is ferromagnetic<sup>51</sup>, but when Ni is substituted by other ions, the ground state magnetic structure changes. However, as shown in Appendix B, the geometry was hardly changed by magnetic order, so calculations were performed with ferromagnetic spin polarization.

Fig. 3 summarizes the screening results. Decreasing vertical axis values indicates smaller contractions and improved cycle performance. Cases that yielded larger structural variation with axes ( $a$ ,  $b$ , and  $c$ ) tilted more than  $2^\circ$  during charging were excluded from the plot [Sr, Zr, Eu, Dy, Ho, Er, Tm, Lu, Pb, K, Rb, La, Ra, Au, Ce, Ca, Ba, Ta, Y, Pm]. Negative  $\Delta d_{\text{ave}}$  values were also excluded because the negative values indicate that the contraction is already larger than that of LNO (positive at 75% charging). Among the 32 elements depicted, Bi and Nb doping are expected to yield the smallest contractions and most significantly improve cycle performance. To investigate thermodynamic stability, the formation energies of the Bi- and Nb-doped systems were calculated. Bi has a high formation energy, so it is expected that Bi cannot be dissolved in LNO. Therefore, we conclude that the best doping element is Nb. (See Appendix C for further details.)

Although it is generally difficult to identify the factors underlying the trends observed in Fig. 3, we performed data analyses using materials informatics, as described below. For the descriptors of  $\Delta d_{\text{ave}}$ , we used 'elemental information of the X substitutes' (including atomic numbers, atomic radii *etc.*) provided on the horizontal axis of Fig. 3. The elemental information was obtained from 'pymatgen' (Python Materials Genomics)<sup>52</sup> to obtain a set of properties, as listed in the left column of Table II. For  $X = \text{Hg}$  and  $X = \text{Tc}$ , incomplete data was available and they were excluded from the regression. As descriptors, we included the 'structural information' (including substituted position of Co, which is another substitute in the system) as listed in the right column.

Less important descriptors were identified by LASSO regression<sup>53</sup>. By excluding these descriptors, we obtained a sparse form of a regression,

$$\begin{aligned} \Delta d_{X,\text{ave}} = & -8.5 \times 10^{-3} \cdot (x \text{ coordinate of X}) \\ & -6.8 \times 10^{-3} \cdot (z \text{ coordinate of Co}) \\ & -2.1 \times 10^{-3} \cdot (\text{covalent radius}) \\ & +1.3 \times 10^{-3} \cdot (x \text{ coordinate of Co}) \\ & +7.8 \times 10^{-4} \cdot (\text{density of solid}) \\ & -4.4 \times 10^{-4} \cdot c \\ & -8.6 \times 10^{-5} \cdot (\text{atomic radius}), \end{aligned} \quad (2)$$

where each descriptor is standardized so that the standardized data set has a mean of 0.0 and standard deviation of 1.0. The regression, Eq. (2), was confirmed to

Elemental information of X	Geometries at discharged state
Atomic number	Lattice constant
Group	Lattice volume
Period	Substituted position of Co
Covalent radius	Substituted position of X
Electronegativity	
First-ionization energy	
Atomic mass	
Atomic radius	
Coefficient of linear thermal expansion	
Solid density	
Electrical resistivity	
Molar volume	
Thermal conductivity	

TABLE II. List of descriptors for the regression of  $\Delta d_{\text{ave}}$ . 'X' denotes the element appearing on the horizontal axis of Fig. 3. The left-hand column lists the properties of X, which were obtained from the 'pymatgen' database<sup>52</sup>.

work fairly well, as shown in Fig. 4. It (vertical axis) reproduced the results obtained by the simulation (horizontal axis) within an RMS error of  $8.3 \times 10^{-3} \text{ \AA}$ .

From the LASSO regression, we identified the quantities that should be considered for designing systems with improved cycle performance. The relevant factors are the substituted positions and densities of X or Co, as they are likely to dominate the charge density at the inter-layer region and contraction of the crystals via inter-layer vdW interactions. Because the regression was based only on the relaxed geometries and densities in the discharged state, we avoided the need for full-simulations including evaluations of the charged state, where it is difficult to consider Li vacancies. Once we are confident in the qualitative observations that the charge density between layers in the discharged state was significant, we will attempt to search for complex compositions (such as substitutions using two elements *etc.*) to achieve further improved performance.

#### IV. CONCLUSION

The  $c$ -axis contractions of LNO when Li ions are desorbed were satisfactorily described by DFT with vdW-XC, but not with PBE. The optimized framework reproduced the H2→H3 'transition' as a sharp drop of the  $c$  length without symmetric transition. Using this framework, we performed a high-throughput screening for ideal combinations of doping substitutes for Co in LNO to minimize the change in  $c$  for improved cycle performance. Nb was the most promising candidates in this study. The computational screening can save significant amounts of time required for the materials screening by experimental syntheses. Using LASSO data analysis, the regression

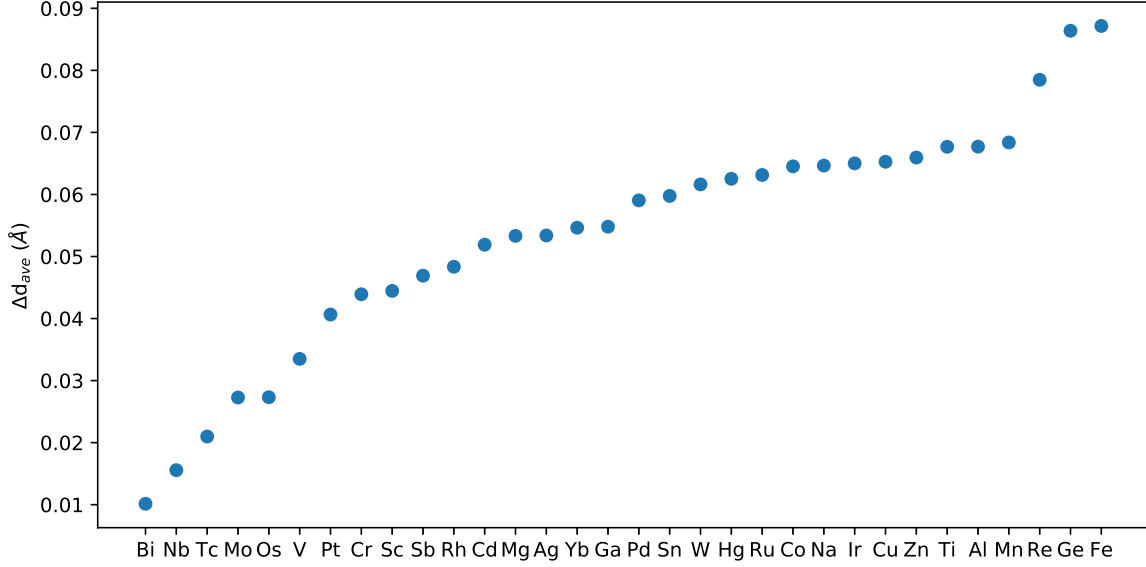


FIG. 3. The  $c$ -axis contractions induced by 75% charging were evaluated in terms of  $\Delta d_{\text{ave}}$ . Lower vertical axis values indicate smaller expected contractions and improved cycle performance. Elements along the horizontal axis are arranged in order of the magnitude of  $\Delta d_{\text{ave}}$ .

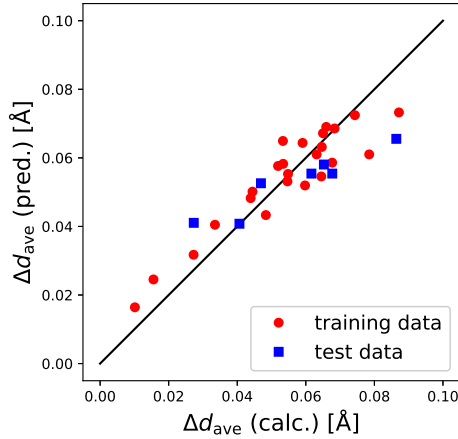


FIG. 4. The performance of the regression given in Eq. (2). The regression (vertical axis) reproduced the simulation results (horizontal axis) fairly well with an RMS error of  $8.3 \times 10^{-3} \text{ \AA}$ .

implied that the charge density between layers was the dominant underlying factor for the contraction.

#### ACKNOWLEDGMENTS

T. Y. would like to thank K. Utimula, T. Kosasa, K. Ryoshi, T. Toma, S. Yoshio, and N. Watanabe for

their fruitful discussions and technical support. The computations in this work were performed using the facilities of the Research Center for Advanced Computing Infrastructure at JAIST. K.H. is grateful for financial support from a KAKENHI grant (17K17762), a Grant-in-Aid for Scientific Research on Innovative Areas (16H06439), the FLAG-SHIP2020 project (MEXT for the computational resources, projects hp180206 and hp180175 at K-computer), PRESTO (JPMJPR16NA) and the Materials research by Information Integration Initiative (MI<sup>2</sup>I) project of the Support Program for Starting Up Innovation Hub from Japan Science and Technology Agency (JST). R.M. is grateful for financial support from MEXT-KAKENHI (project JP16KK0097), the FLAG-SHIP2020 project (MEXT for the computational resources, projects hp180206 and hp180175 at K-computer), and the Air Force Office of Scientific Research (AFOSR-AOARD/FA2386-17-1-4049)

#### Appendix A: Calculated structures

We show the calculated structures for doped systems in Fig. 5.

#### Appendix B: Magnetic structure

We summarize energy and lattice parameters for ferromagnetic, antiferromagnetic stacking of spin-ferro order



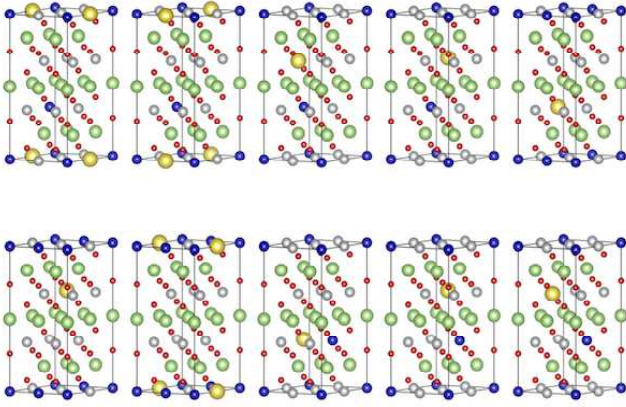


FIG. 5. 10 symmetrically different doped systems. Green, red, gray, blue, and yellow balls show Li, O, Ni, Co, and X, respectively

Ni layers, and non magnetic LNO in Table III.

### Appendix C: Formation energy

Formation energy  $E_F$  is defined as,

$$E_F = E(\text{LiNi}_{0.75}\text{Co}_{0.17}\text{X}_{0.08}\text{O}_2) - (1 - c)E(\text{LiNi}_{0.83}\text{Co}_{0.17}\text{O}_2) - cE(\text{LiX}_{0.83}\text{Co}_{0.17}\text{O}_2) \quad (\text{C1})$$

where  $E$  and  $c = 0.1$  denote the total energy and concentration of X. We investigate the formation energy for Bi and Nb doped system. The formation energy is 0.848 eV for former and -1.993 eV for later.

- <sup>1</sup> K. Kang, Y. S. Meng, J. Br  ger, C. P. Grey, and G. Ceder, *Science* **311**, 977 (2006).
- <sup>2</sup> A. Manthiram, A. Vadivel Murugan, A. Sarkar, and T. Muraliganth, *Energy Environ. Sci.* **1**, 621 (2008).
- <sup>3</sup> C. S. Yoon, D.-W. Jun, S.-T. Myung, and Y.-K. Sun, *ACS Energy Lett.* **2**, 1150 (2017).
- <sup>4</sup> Y. Gao, M. V. Yakovleva, and W. B. Ebner, *Electrochem. Solid-State Lett.* **1**, 117 (1998).
- <sup>5</sup> J. Dahn, E. Fuller, M. Obrovac, and U. von Sacken, *Solid State Ionics* **69**, 265 (1994).
- <sup>6</sup> N. Nitta, F. Wu, J. T. Lee, and G. Yushin, *Mat. Today* **18**, 252 (2015).
- <sup>7</sup> K. Mizushima, P. Jones, P. Wiseman, and J. Goodenough, *Mater. Res. Bull.* **15**, 783 (1980).
- <sup>8</sup> S.-T. Myung, F. Maglia, K.-J. Park, C. S. Yoon, P. Lamp, S.-J. Kim, and Y.-K. Sun, *ACS Energy Lett.* **2**, 196 (2017).
- <sup>9</sup> J. Dahn, U. von Sacken, and C. Michal, *Solid State Ionics* **44**, 87 (1990).
- <sup>10</sup> T. Ohzuku, A. Ueda, and M. Nakayama, *J. Electrochem. Soc.* **140**, 1862 (1993).
- <sup>11</sup> S. Yamada, M. Fujiwara, and M. Kanda, *J. Power Sources* **54**, 209 (1995).
- <sup>12</sup> A. Rougier, P. Gravereau, and C. Delmas, *J. Electrochem. Soc.* **143**, 1168 (1996).
- <sup>13</sup> H. Arai, S. Okada, Y. Sakurai, and J. ichi Yamaki, *Solid State Ionics* **95**, 275 (1997).
- <sup>14</sup> Y. S. Lee, Y. K. Sun, and K. S. Nahm, *Solid State Ionics* **118**, 159 (1999).
- <sup>15</sup> R. Kanno, H. Kubo, Y. Kawamoto, T. Kamiyama, F. Izumi, Y. Takeda, and M. Takano, *J. Solid State Chem.* **110**, 216 (1994).
- <sup>16</sup> W. Li, J. N. Reimers, and J. R. Dahn, *Phys. Rev. B: Condens. Matter Mater. Phys.* **46**, 3236 (1992).
- <sup>17</sup> M. Guilmard, A. Rougier, M. Gr  ne, L. Croguennec, and C. Delmas, *J. Power Sources* **115**, 305 (2003).
- <sup>18</sup> M. Guilmard, L. Croguennec, D. Denux, and C. Delmas, *Chem. Mater.* **15**, 4476 (2003).
- <sup>19</sup> C. Poull  rie, L. Croguennec, P. Biensan, P. Willmann, and C. Delmas, *J. Electrochem. Soc.* **147**, 2061 (2000).
- <sup>20</sup> R. Sathiyamoorthi, P. Shakkthivel, S. Ramalakshmi, and Y.-G. Shul, *J. Power Sources* **171**, 922 (2007).
- <sup>21</sup> H. Kondo, Y. Takeuchi, T. Sasaki, S. Kawauchi, Y. Itou, O. Hiruta, C. Okuda, M. Yonemura, T. Kamiyama, and Y. Ukyo, *J. Power Sources* **174**, 1131 (2007).
- <sup>22</sup> J. Cho, H. Jung, Y. Park, G. Kim, and H. S. Lim, *J. Electrochem. Soc.* **147**, 15 (2000).
- <sup>23</sup> C. Delmas, I. Saadoune, and A. Rougier, *J. Power Sources* **44**, 595 (1993).
- <sup>24</sup> I. Saadoune and C. Delmas, *J. Mater. Chem.* **6**, 193 (1996).
- <sup>25</sup> E. Rossen, C. Jones, and J. Dahn, *Solid State Ionics* **57**, 311 (1992).
- <sup>26</sup> S. Venkatraman and A. Manthiram, *Chem. Mater.* **15**, 5003 (2003).
- <sup>27</sup> P. Mohan and G. P. Kalaignan, *J. Electroceramics* **31**, 210 (2013).
- <sup>28</sup> P. Mohan and G. P. Kalaignan, *J. Nanoscience and Nanotechnology* **14**, 5278 (2014).
- <sup>29</sup> S. N. Kwon, M. Y. Song, and H. R. Park, *Ceram. Int.* **40**, 14141 (2014).
- <sup>30</sup> H.-S. Kim, T.-K. Ko, B.-K. Na, W. I. Cho, and B. W. Chao, *J. Power Sources* **138**, 232 (2004).
- <sup>31</sup> C. S. Yoon, M.-J. Choi, D.-W. Jun, Q. Zhang, P. Kag-hazchi, K.-H. Kim, and Y.-K. Sun, *Chem. Mater.* **30**, 1808 (2018).
- <sup>32</sup> C. S. Yoon, U.-H. Kim, G.-T. Park, S. J. Kim, K.-H. Kim, J. Kim, and Y.-K. Sun, *ACS Energy Lett.* **3**, 1634 (2018).
- <sup>33</sup> H. Kim, A. Choi, S. W. Doo, J. Lim, Y. Kim, and K. T. Lee, *J. Electrochem. Soc.* **165**, A201 (2018).
- <sup>34</sup> G. G. Amatucci, J. M. Tarascon, and L. C. Klein, *J. Electrochem. Soc.* **143**, 1114 (1996).
- <sup>35</sup> M. Nishijima, T. Ootani, Y. Kamimura, T. Sueki, S. Esaki, S. Murai, K. Fujita, K. Tanaka, K. Ohira, Y. Koyama, and I. Tanaka, *Nat. Comm.* **5**, 4553 (2014).
- <sup>36</sup> G. Kresse and J. Furthm  ller, *Phys. Rev. B: Condens. Matter Mater. Phys.* **54**, 11169 (1996).
- <sup>37</sup> G. Kresse and J. Furthm  ller, *Comput. Mater. Sci.* **6**, 15 (1996).

Magnetic structure	Energy (meV)	$a(\text{\AA})$	$c(\text{\AA})$
Ferromagnetic order	0	2.87	14.04
Antiferromagnetic order	19	2.88	14.06
Non magnetic order	148	2.87	14.00

TABLE III. Relative energies and structural parameters. The zero for the energy is chosen to be ferromagnetic order.

- <sup>38</sup> J. Klimeš, D. R. Bowler, and A. Michaelides, Phys. Rev. B: Condens. Matter Mater. Phys. **83**, 195131 (2011).
- <sup>39</sup> J. Klimeš, D. R. Bowler, and A. Michaelides, J. Phys.: Cond. Matt. **22**, 022201 (2010).
- <sup>40</sup> J. P. Perdew, K. Burke, and M. Ernzerhof, Phys. Rev. Lett. **77**, 3865 (1996).
- <sup>41</sup> S. Grimme, J. Antony, S. Ehrlich, and H. Krieg, J. Chem. Phys. **132**, 154104 (2010).
- <sup>42</sup> A. Chakraborty, M. Dixit, and D. T. Major, npj Comput. Mater. **4**, 60 (2018).
- <sup>43</sup> M. Aykol, S. Kim, and C. Wolverton, J. Phys. Chem. C **119**, 19053 (2015).
- <sup>44</sup> A. Tamura, S. Takai, T. Yabutsuka, and T. Yao, J. Electrochem. Soc. **164**, A1514 (2017).
- <sup>45</sup> F. Zhou, M. Cococcioni, C. A. Marianetti, D. Morgan, and G. Ceder, Phys. Rev. B: Condens. Matter Mater. Phys. **70**, 235121 (2004).
- <sup>46</sup> C. N. M. Ouma, M. Z. Mapelu, N. W. Makau, G. O. Amolo, and R. Maezono, Phys. Rev. B: Condens. Matter Mater. Phys. **86**, 104115 (2012).
- <sup>47</sup> C. Kittel, *Introduction to Solid State Physics*, 8th ed. (John Wiley & Sons, Inc., New York, 2004).
- <sup>48</sup> K. Hongo and R. Maezono, J. Chem. Theory Comput. **13**, 5217 (2017).
- <sup>49</sup> Y. Yao and Y. Kanai, J. Chem. Phys. **146**, 224105 (2017).
- <sup>50</sup> F. Schipper, E. M. Erickson, C. Erk, J.-Y. Shin, F. F. Chesneau, and D. Aurbach, J. Electrochem. Soc. **164**, A6220 (2017).
- <sup>51</sup> V. I. Anisimov, J. Zaanen, and O. K. Andersen, Phys. Rev. B: Condens. Matter Mater. Phys. **44**, 943 (1991).
- <sup>52</sup> S. P. Ong, W. D. Richards, A. Jain, G. Hautier, M. Kocher, S. Cholia, D. Gunter, V. L. Chevrier, K. A. Persson, and G. Ceder, Comput. Mater. Sci. **68**, 314 (2013).
- <sup>53</sup> R. Tibshirani, J. R. Stat. Soc. Ser. **58**, 267 (1996).